Construction and Building Materials 538 (2026) 147197

Contents lists available at ScienceDirect

Construction and Building Materials

journal homepage: www.elsevier.com/locate/conbuildmat

Experimental and numerical fracture behaviour of CNC-manufactured OSB beams

Christian Málaga-Chuquitaype [a,*], Opeyemi Ogunkuade [a], Zilan Zhang [a], Gabriele Granello [b]

[a] Department of Civil and Environmental Engineering, Imperial College London, London, UK
[b] Open Systems Lab, London, UK

ARTICLE INFO

Keywords:
Digital fabrication
OSB
Interlocking plates
All-timber joints
WikiHouse

ABSTRACT

The WikiHouse Skylark system is an open-source, CNC-manufactured interlocking-plate structural system without metal connectors with strong prospects for sustainable prefabricated housing. We present the first experimental and numerical study of full-scale Skylark beams manufactured from OSB (oriented strand board); a material of greater circularity potential than the plywood for which the system was originally developed. Nine large-scale specimens across three cross-sections, heights, and spans were tested under monotonic four-point bending to failure. Failure is consistently governed by the castellated joints at the bottom flange, identifying this as the critical design region for the updated Skylark geometry. Analytical and finite element models are developed and show good agreement with the observed responses. Collectively, the results provide the first full-scale validation of the structural performance of OSB Skylark beams and establish a quantitative basis for their use in sustainable prefabricated housing.

1. Introduction

Modular wood-based construction systems are attracting increasing interest as the construction sector seeks environmentally responsible and scalable solutions to address the growing global demand for housing [1,2]. Wood and wood-based materials are particularly well suited to this context due to their renewability, low embodied carbon, and favourable strength-to-weight ratio. When combined with off-site manufacturing and modular design strategies, wood-based systems can contribute to improved construction efficiency, reduced waste, and is expected to enhance the affordability and whole life carbon emissions [3].

Among the various approaches to modular fabrication, computer-numerical-control (CNC) machining has played a key role within the timber and wood-based industries [4]. Advances in digital design and manufacturing workflows have enabled CNC fabrication to support the development of integrated structural systems where three-dimensional digital models are directly linked to fabrication processes, allowing high levels of standardisation while retaining flexibility in architectural design.

A notable outcome of this development is the emergence of interlocking plate-based timber systems, in which structural elements are assembled from CNC-cut panels. The structural integrity of joints in these systems relies on geometric interlock, contact, and friction for load transfer, rather than conventional metal fasteners [5,6]. By minimising or eliminating screws, bolts, and nails, these systems offer potential advantages in terms of construction speed, cost efficiency, and adaptability, as well as improved disassembly and reuse potential. However, the structural behaviour of such systems is often governed by joint performance, which may introduce significant compliance, nonlinear behaviour, and partial contact between connected panels. As a result, experimental validation at the structural element scale remains essential. In this context, Rad et al. [7] examined the effects of angles between the panels and the grain direction on the connection response, concluding that the fibre direction played a key role in the response of these joints. Besides, numerical models, both simplified [8] and more sophisticated [9], have also been used to estimate the response of interlocking joints towards their practical implementation.

One of the most prominent open-source examples of an interlocking timber construction system is WikiHouse, and in particular its Skylark structural platform [10]. The Skylark system has been developed to enable locally manufactured, digitally fabricated housing using widely available CNC equipment. Previous experimental investigations on five Skylark beams fabricated from plywood have demonstrated ductile behaviour under bending and highlighted the critical influence of joint flexibility on global stiffness and deflection response [11]. These findings underline the importance of accounting for joint behaviour when assessing the structural performance of interlocking timber elements and stressed the need for additional testing.

* Correspondence to: Room 322, Skempton Building, South Kensington Campus, SW7 2AZ, UK.
E-mail address: c.malaga@imperial.ac.uk (C. Málaga-Chuquitaype).

https://doi.org/10.1016/j.conbuildmat.2026.147197
Received 24 March 2026; Received in revised form 4 June 2026; Accepted 21 June 2026
Available online 2 July 2026
0950-0618/© 2026 The Author(s). Published by Elsevier Ltd. This is an open access article under the CC BY license (http://creativecommons.org/licenses/by/4.0/).

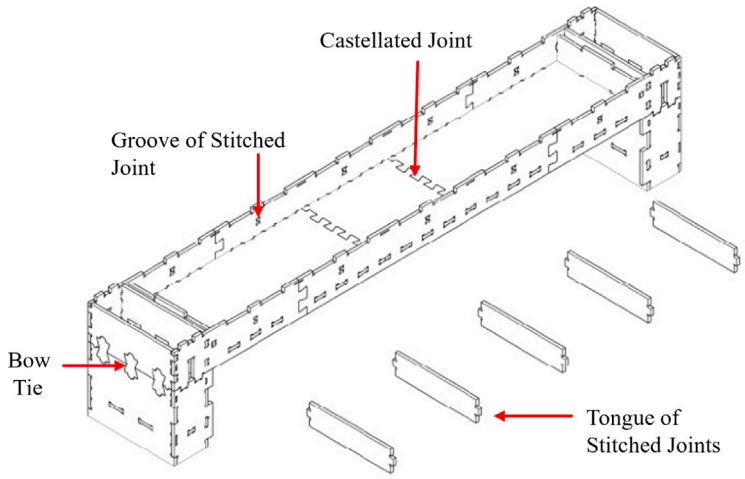


Fig. 1. Components and general view of a typical Skylark beam.

While early development and validation of the Skylark system focused primarily on plywood panels, more recent iterations have explored the use of alternative engineered wood products with improved accessibility and circularity potential, such as oriented strand board (OSB). OSB differs from plywood in terms of material composition, strand orientation, and anisotropy, which may significantly influence both global member behaviour and local joint performance [12]. Although OSB is widely used in timber construction for sheathing and decking applications, its use in load-bearing, interlocking structural systems remains relatively under-explored, particularly at the full-scale structural element level.

Against this background, this paper makes the following specific contributions:

- It presents the first experimental study of full-scale CNC-manufactured OSB Skylark beams (Fig. 1), extending prior work conducted on plywood to a material of greater circularity and accessibility potential.
- It investigates the updated Skylark joint geometry under realistic structural conditions across nine specimens covering three section heights and span configurations under monotonic four-point bending.
- It identifies the castellated joints at the bottom flange as the consistently governing failure region, establishing this as the critical design zone for OSB Skylark beams under bending.
- It demonstrates that analytical and finite element models, including semi-rigid rotational joint representations and fracture initiation models, capture the observed stiffness and load–displacement behaviour with good accuracy, providing a validated modelling framework for design studies.

The remainder of this paper is organised as follows. Section 2 describes the experimental programme, including the specimen geometry, material properties, and test setup. Section 3 presents the experimental results and discusses the observed failure modes including the presentation of an analytical framework for the preliminary estimation of deformations. Section 4 describes the finite element modelling strategy adopted and the approach followed for the estimation of structural capacity based on fracture initiation. Section 5 presents a comparison between the numerical predictions and the experimental results. Finally, Section 6 summarises the conclusions of this work. Together, the experimental and numerical evidence presented advances the fundamental understanding of interlocking timber structural behaviour and demonstrates the viability of CNC-cut OSB Skylark beams as a structurally sound and sustainable solution for prefabricated modular housing.

2. Experimental investigation

2.1. Background

The WikiHouse project emerged in 2014 as a digitally driven, open-source approach to timber construction. The system is based on the fabrication of hollow structural components—such as beams, columns, and connection elements—produced, originally from flat plywood panels using CNC machining. These components are designed to be assembled on site to form complete residential buildings. Production of WikiHouse components relies on standard three-axis CNC equipment. This manufacturing strategy enables a high degree of repeatability while remaining compatible with relatively simple fabrication infrastructure.

In 2020, the WikiHouse initiative introduced a revised structural platform known as Skylark. The primary objective of this system was to rationalise structural components and manufacturing processes, thereby increasing efficiency and reducing both material waste and overall production costs. Skylark is organised around a catalogue of standardised components that can be configured in multiple ways, allowing a wide range of building layouts to be generated from a limited set of components.

More recently, motivated by its widespread availability within the UK, reduced reliance on imported materials, and potential benefits in terms of cost, supply-chain resilience, and circularity, the WikiHouse project has begun exploring the use of locally sourced British oriented strand board (OSB) as an alternative to plywood for the fabrication of structural components. In parallel, the Skylark system has undergone refinement of its joint geometry and connection layout, aimed at improving load transfer, assembly robustness, and overall structural performance. The beams investigated in the present study incorporate these updated features (Figs. 1 and 2). The experimental programme reported herein therefore provides a first assessment of the bending behaviour and failure mechanisms of these revised WikiHouse Skylark OSB beams.

2.2. Description of specimens

Nine specimens involving three different beam sizes were tested at the Structures Laboratory of Imperial College London. These include three L specimens, three S specimens and three XXS specimens. The specimens were made of Sterling OSB3, which properties are reported in [12] and summarised in Table 1. The OSB panel thickness was 18 mm and a 0.25 mm fabrication tolerance was used. All specimens had 8 castellated joints while the number of stitched joints was 94, 116 and 140 for the XXS, S and L specimens, respectively.



Fig. 2. Skylark beam specimen after testing.

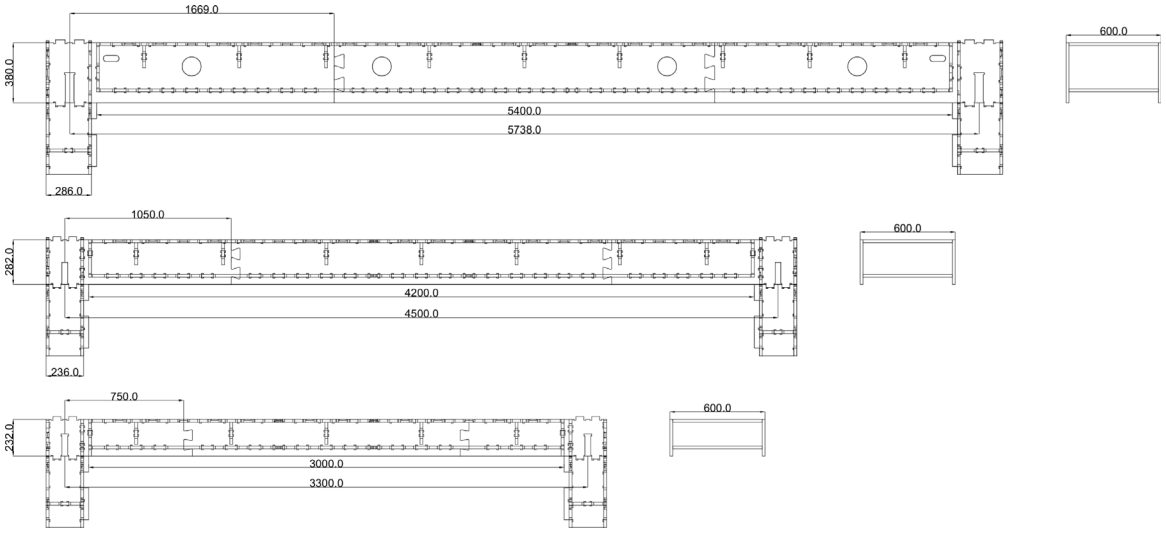


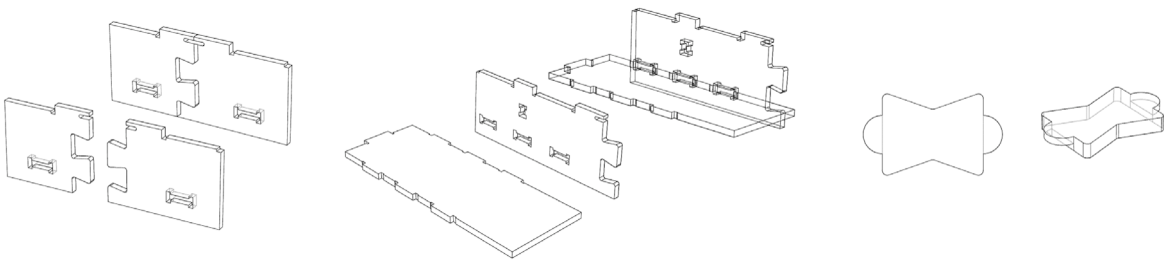
Fig. 3. Lateral and section views of specimens tested and their dimensions in mm. Specimen L (top), Specimen S (middle), Specimen XXS (bottom).

Table 1
Summary of material properties for the OSB used in the specimens under consideration. All properties, except the bending modulus that is taken from the material specification document, are taken from [12].

Property	Value
Average compression strength [MPa]	11.8
Elastic compression modulus [MPa]	2755
Average tension strength [MPa]	8.3
Elastic tension modulus [MPa]	3111
Average bending modulus [MPa]	4930

The dimensions of the specimens tested are shown in Fig. 3. All specimens were 600 mm wide and included a beam–column joint at both ends together with a short stud placed on the strong-floor acting as simple support. It is noted that whilst the span-to-depth ratios adopted fall below the minimum of 18 recommended by EN 408 [13], the response of these beams is joint-dominated rather than shear-dominated, as evidenced later in this paper. Lateral movement of the supports was continuously monitored through the test and confirmed to be negligible. L specimens had a span of 5.7 m (column centre to column centre), and included 380-mm deep beams. S specimens had a span of 4.5 m (centre to centre), and were made of 278-mm deep beams. XXS specimens had 232-mm deep beams and a span of 3.3 m (centre to centre). The specimens were assembled by attaching the CNC-cut panels through their interlocking joints, without the use of specialist tools or metal fasteners. Structural continuity was achieved through a limited number of joint typologies which play a primary role in the system's response and are presented in Fig. 4.

The first category of joints consists of the castellated or dovetail type, which are used to connect shorter panel segments end-to-end in order to form longer structural members. Hence, load transfer occurs between panels arranged in parallel planes, with the interlocking geometry providing continuity along the length of the element. Castellated joints are used in both beam flanges and webs, where they enable the



(a) Castellated dovetail joints. (b) Stitched joint. (c) Bow-tie joint.

Fig. 4. Different joint types present in Skylark beams.

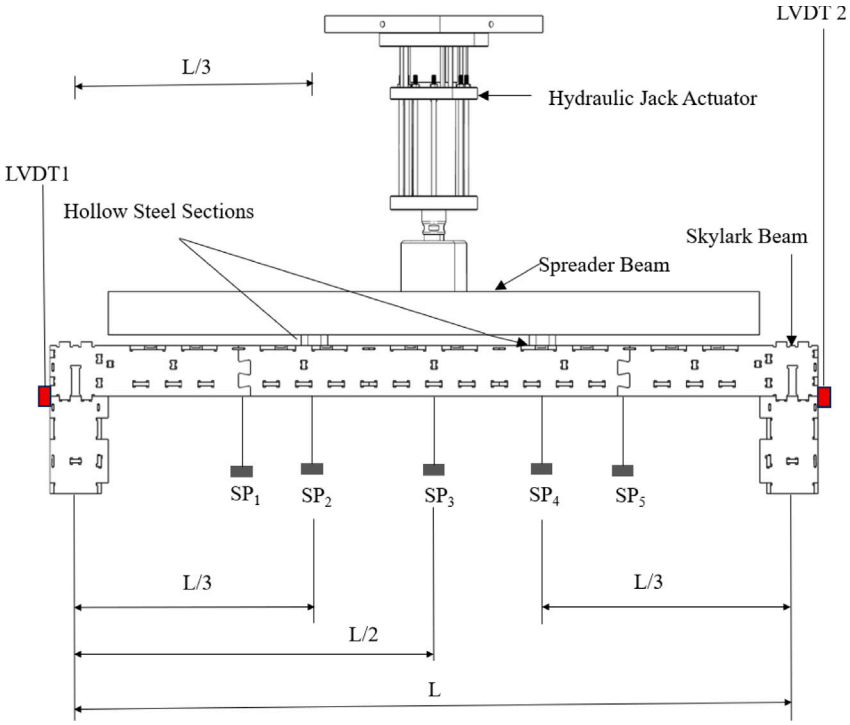


Fig. 5. Schematic diagram of four-point bending test set-up. Note: SP1 and SP5 are placed at the castellated joint to monitor the opening of joint, which can vary from specimen to specimen.

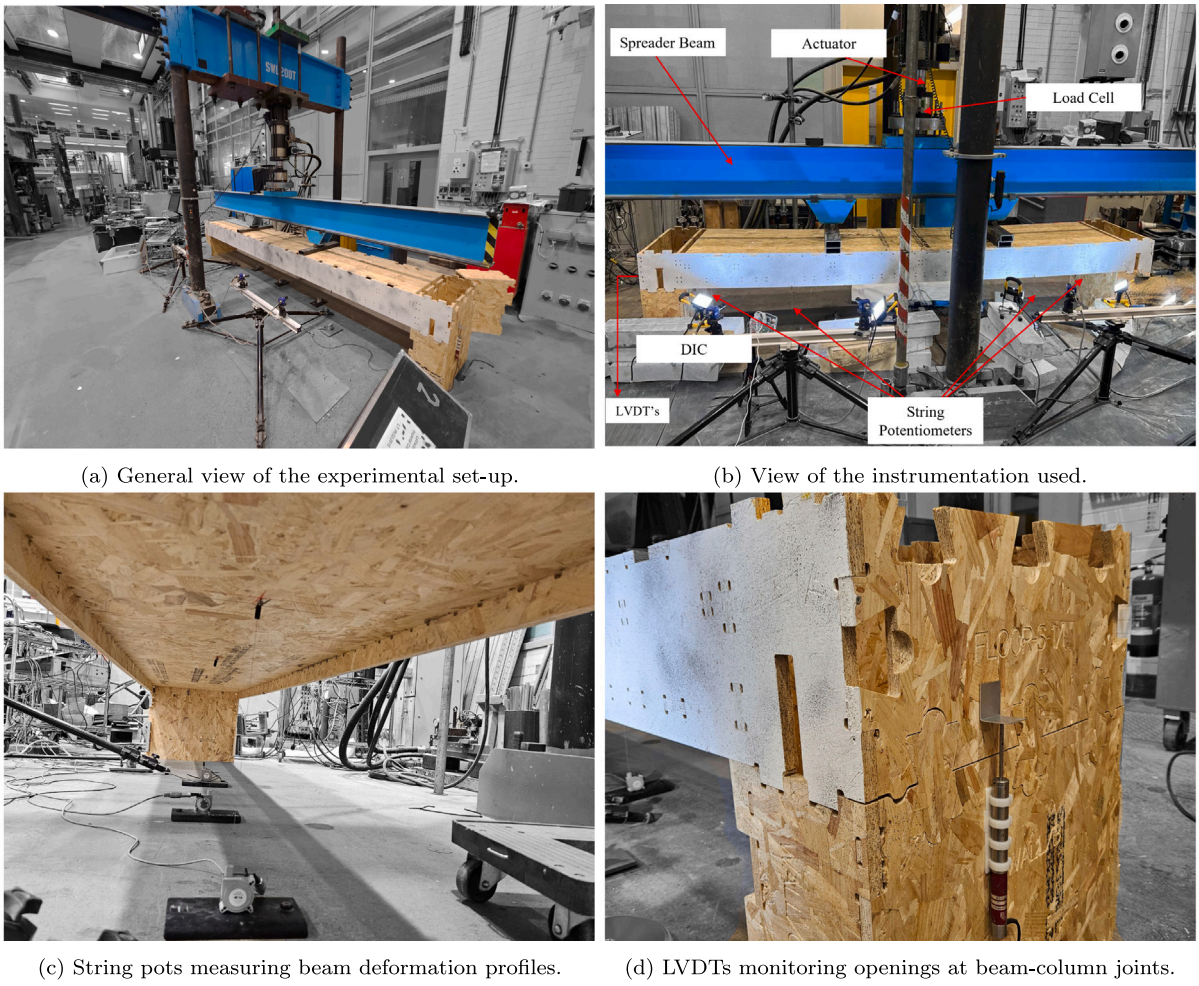
construction of members exceeding the dimensions of individual panels. The second category comprises stitched joints, which are employed to form hollow box-type components by connecting panels arranged in mutually orthogonal planes. These joints enable the creation of closed sections by linking vertical and horizontal elements and are commonly found at interfaces such as those between web and flanges. Finally, bow-tie joints consist of a double-tapered OSB element whose narrow central waist interlocks with corresponding recesses in the adjacent panels. Their geometry provides in plane restraint through geometric interlock.

2.3. Experimental set-up

The arrangement used for testing the beam-to-column connections is shown schematically in Fig. 5. A 250 kN hydraulic actuator operating in displacement control was used to apply vertical forces through a 5 m long UB 305 × 102 × 33 spreader beam and two 10 × 10 × 600 mm hollow core rectangular steel profiles placed at L/3 from the end supports, as shown in Fig. 5, where L is the span of the specimens.

The instrumentation employed can be seen in Figs. 5 and 6. Vertical displacements and corresponding forces were recorded by the load cell and displacement transducer incorporated within the actuator. In addition, the specimen displacement profile was tracked via five string potentiometers (SP) and two Linear Variable Differential Transformers (LVDT). Vertical displacements of the beams were recorded using SPs, while LVDTs were installed to monitor relative opening between the beam and column interfaces. Furthermore, two high-resolution cameras were employed to capture strain development through digital image correlation (DIC). Owing to the limited field of view of the camera setup, which covered approximately one metre of the specimen length, the camera locations were adjusted between individual tests.

The loading protocol was adapted from the recommendations of EN 1380:2009 [14]. This choice was motivated by the preponderant role of the inter-panel connections in governing the global response of the specimens, which makes each full-scale beam test effectively equivalent to a system-level connector-focused test. The load–unload–reload sequence prescribed by EN 1380:2009 was therefore adopted to characterise both the initial stiffness and the response during unloading and reloading. The protocol comprised three stages: (i) monotonic loading up to 40% of the estimated peak force, (ii) unloading down to 10% of the estimated peak force, with a one-minute dwell period between the two branches, and (iii) subsequent monotonic reloading until failure. The reference value for the estimated peak force for each specimen group was obtained from the analytical model proposed



(a) General view of the experimental set-up.

(b) View of the instrumentation used.

(c) String pots measuring beam deformation profiles.

(d) LVDTs monitoring openings at beam-column joints.

Fig. 6. Experimental set-up and instrumentation.

in [11]. All tests were carried out under displacement control at a constant actuator rate of 3 mm/min, with the actuator force used as the control quantity for the definition of the 40% and 10% reference levels. The forces and corresponding mid-span displacements at these two reference levels were used to compute the initial elastic stiffness k_{el} reported in Section 3.

3. Experimental results and observations

The main response parameters obtained from the tests are summarised in Table 2, and the key results are presented in Figs. 7, 8 and 9 in terms of total force versus mid-span deflection relationships. Peak forces, F_{max}, were obtained directly from the maximum attained force in the actuator; while corresponding the moment capacity, M_{max}, was calculated as:

$$M_{max} = \frac{F_{max} L}{6} \tag{1}$$

considering a span L, measured centre-to-centre. Likewise, the stiffness reported in Table 2, k_{el} was calculated as:

$$k_{el} = \frac{F_{40\%} - F_{10\%}}{d_{40\%} - d_{10\%}} \tag{2}$$

where $F_{40\%}$ and $F_{10\%}$ are the forces corresponding to 40% and 10% of the beam's total strength, and $d_{40\%}$ and $d_{10\%}$ their corresponding mid-span deflection values.

Table 2
Summary of the experimental results, where F_{max} is the maximum force, k_{el} is the elastic stiffness, L is the span measured centre-to-centre and M_{max} is the moment capacity.

Specimen	F_{max} (kN)	k_{el} (kN/mm)	L (m)	M_{max} (kNm)
XXS-1	12.3	0.486	3.3	6.8
XXS-2	12.0	0.489	3.3	6.6
XXS-3	13.1	0.491	3.3	7.2
	12.5	0.488	3.3	6.9
S-1	12.3	0.385	4.5	9.2
S-2	10.9	0.376	4.5	8.1
S-3	9.0	0.234	4.5	6.8
	10.7	0.332	4.5	8.0
L-1	17.5	0.460	5.7	16.6
L-2	17.7	0.447	5.7	16.8
L-3	18.8	0.437	5.7	17.9
	18.0	0.448	5.7	17.1

3.1. Force-displacement curves

It is clear from the force–displacement curves presented in Figs. 7, 8 and 9 that all specimens experienced brittle failure modes, which contrasts with the observations of [11] on the first generation of Wiki-House beams made from plywood. Despite this, a good repeatability is achieved leading to very low Coefficient of Variation (COV) in elastic stiffness ranging between a minimum of 0.005 for XXS specimens to

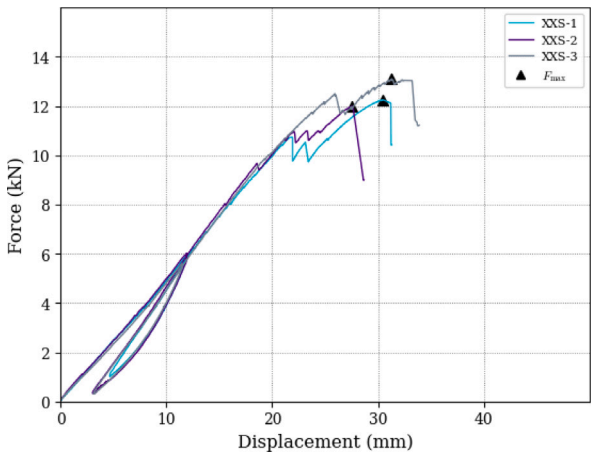


Fig. 7. Force versus displacement relationships of XXS specimens.

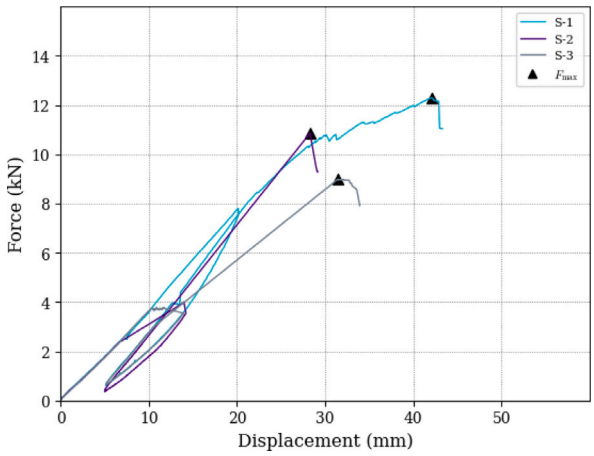


Fig. 8. Force versus displacement relationships of S specimens.

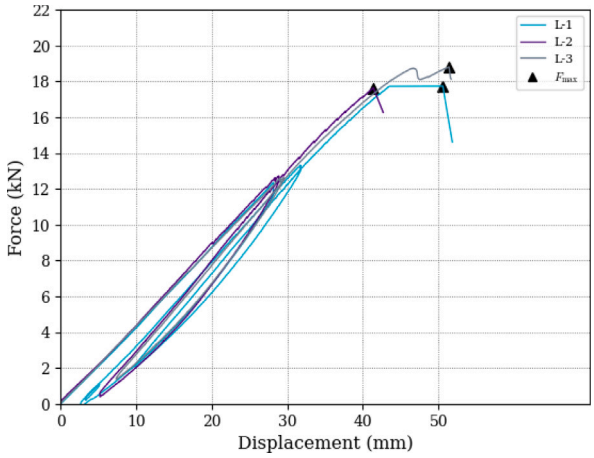


Fig. 9. Force versus displacement relationships of L specimens.

0.026 for L specimens. Relatively low COVs are also observed for peak values, in the order of 0.05 across all specimens. Also shown in Figs. 7, 8 and 9, the unload-reload cycles follow a different path than the original loading branch but always reach the same point at which the original cycle unloaded.

XXS specimens reached a maximum force, F_{max}, of 12.5 kN, in average, with a corresponding moment capacity of 6.9 kNm. Similarly, S specimens reached an average maximum force of 10.7 kN (average moment capacity of 8.0 kNm). And L specimens reached a maximum force of 18.0 kN, in average (average maximum moment equal to 17.1 kNm).

3.2. Failure mechanisms

As noted before, all specimens failed in a similar brittle manner with failure initiating at mid-span. The failure mechanism observed can be further discussed with reference to Figs. 10 to 12. Failure initiated at the castellated joint in the bottom flange of the specimens. Fig. 10 shows the damage and tensile fracture observed in these joints during the post-test examination. Subsequently, failure quickly progressed to the top flange to web connection (Fig. 11), where out of plane deformation due to tensile fracture was observed. This was in many cases accompanied by localised failure of the stitch joints near the two thirds of the span. Also, a progressive accumulation of column uplift was observed generating uneven contact and distortions (Fig. 12) towards the end of the tests. This progression of failure was corroborated with the Finite Element analysis as will be discussed later.

In the previous tests with plywood [11], a ductile failure mode was observed. Such ductile failure was due to the local compression of the bottom tab against the bottom flange of the beam which can be developed because the bottom part of the web can hold the tension until the tab fails in compression. However, since OSB has a significant weaker tensile strength (8.3 MPA vs 18.5 MPa of plywood), the bottom part of the web starts failing in tension before the tabs starts yielding in compression in this study. This phenomenon is particularly visible in specimens XXS and XS because the distance between the bottom flange and the end of the web is smaller. Therefore, the combination of lower mechanical properties and smaller flange to bottom distance make the fragile failure mode triggering earlier that the ductile one.

3.3. Deflection and joint rotational stiffness

The deflected shapes obtained from the linear transducers at different stages of deformation are presented in Figs. 13 to 15 for all specimens tested. Results are plotted for deflections associated with vertical force levels equal to 20%, 40% and 90% of the maximum capacity, to illustrate the evolution of the deformations along the beams.

As expected, and as previously noted by [11] for plywood beams, the displacement measurements demonstrate that Skylark beams do not bend monolithically but the castellated joints in the webs play a key role on the beams deformed shape.

To account for the joint effects, the beams can be idealised as simply supported with rotational springs in correspondence of the dovetail joints, as schematically presented in Fig. 16. Hence, by using Euler–Bernoulli theory, the following equation can be easily derived:

$$v(x) = \begin{cases} -\frac{F}{6EI}x^3 + \left(\frac{FbL}{2EI} - \frac{Fb^2}{2EI} + \frac{FL_j}{k_r}\right)x & x \le L_j \\ -\frac{F}{6EI}x^3 + \left(\frac{FbL}{2EI} - \frac{Fb^2}{2EI}\right)x + \frac{FL_j^2}{k_r} & L_j \le x \le b \\ -\frac{Fb}{2EI}x^2 + \frac{FbL}{2EI}x - \frac{Fb^3}{6EI} + \frac{FL_j^2}{k_r} & b \le x \le 0.5L \end{cases} \quad (3)$$

where E is the flexural elastic modulus of the material (i.e., 4930 MPa), I is the second moment of area, F is half of the force at the actuator ($F = F_{max}/2$, considering the reaction of a simply supported beam under four-point bending), b is the distance between the support and point of application of the force F, L_j is the distance between the support and the dovetail castellated joint and k_r is the dovetail joint rotational stiffness.

The rotational stiffness of the dovetail joint, k_r, was estimated directly from the full-field displacement measurements obtained through Digital Image Correlation (DIC). The procedure adopted, summarised in Fig. 17, exploits the fact that, away from the local stress concentrations

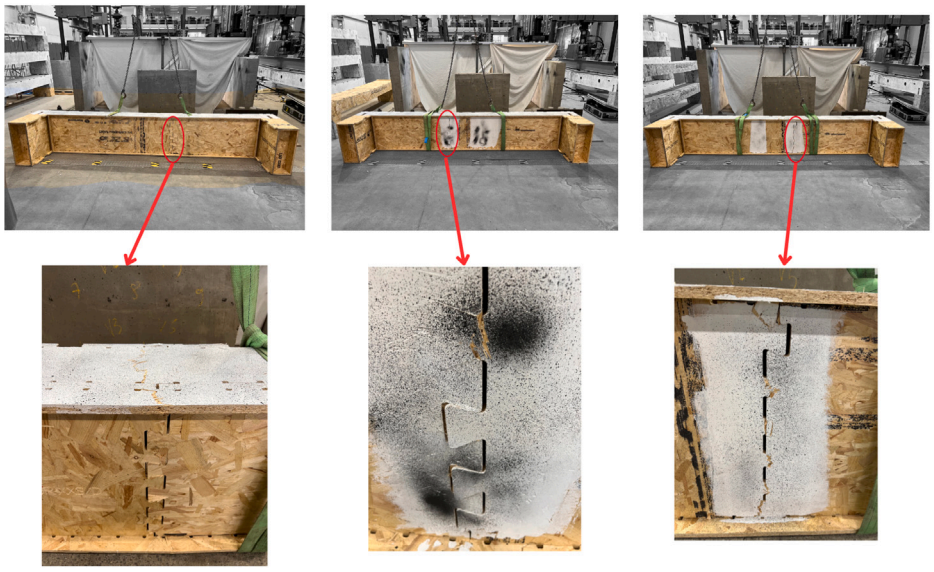
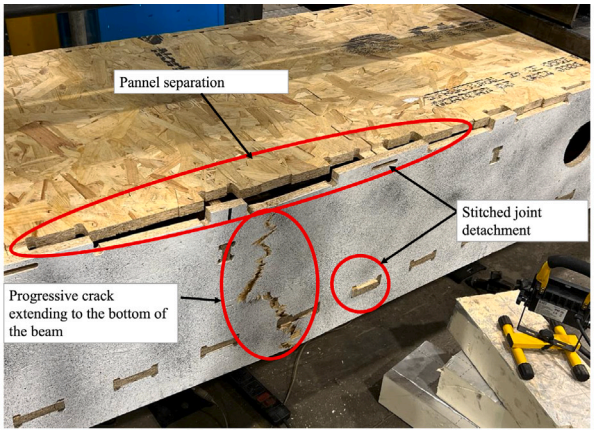
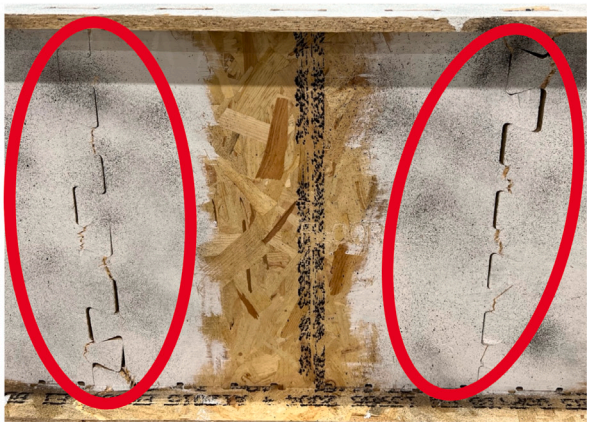


Fig. 10. Failure of beams XXS at castellated joints in the bottom flange.

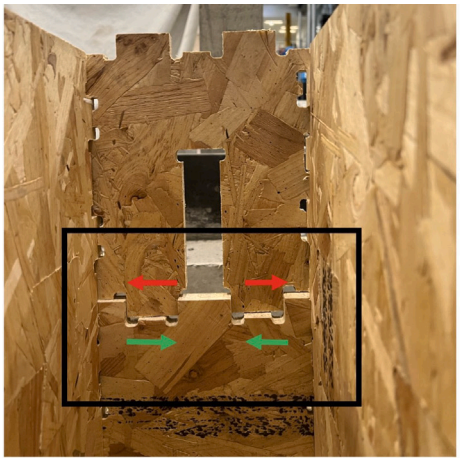


(a) Failure at mid-span involving tensile fracture of the beam web and out of plane buckling.

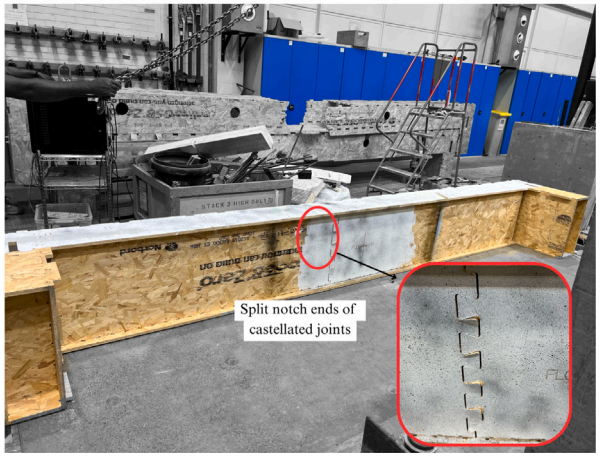


(b) Failure at bottom flange castellated joint.

Fig. 11. Failure at mid-span, followed by progressive cracks and detachment of panels in the lateral faces of the beam.

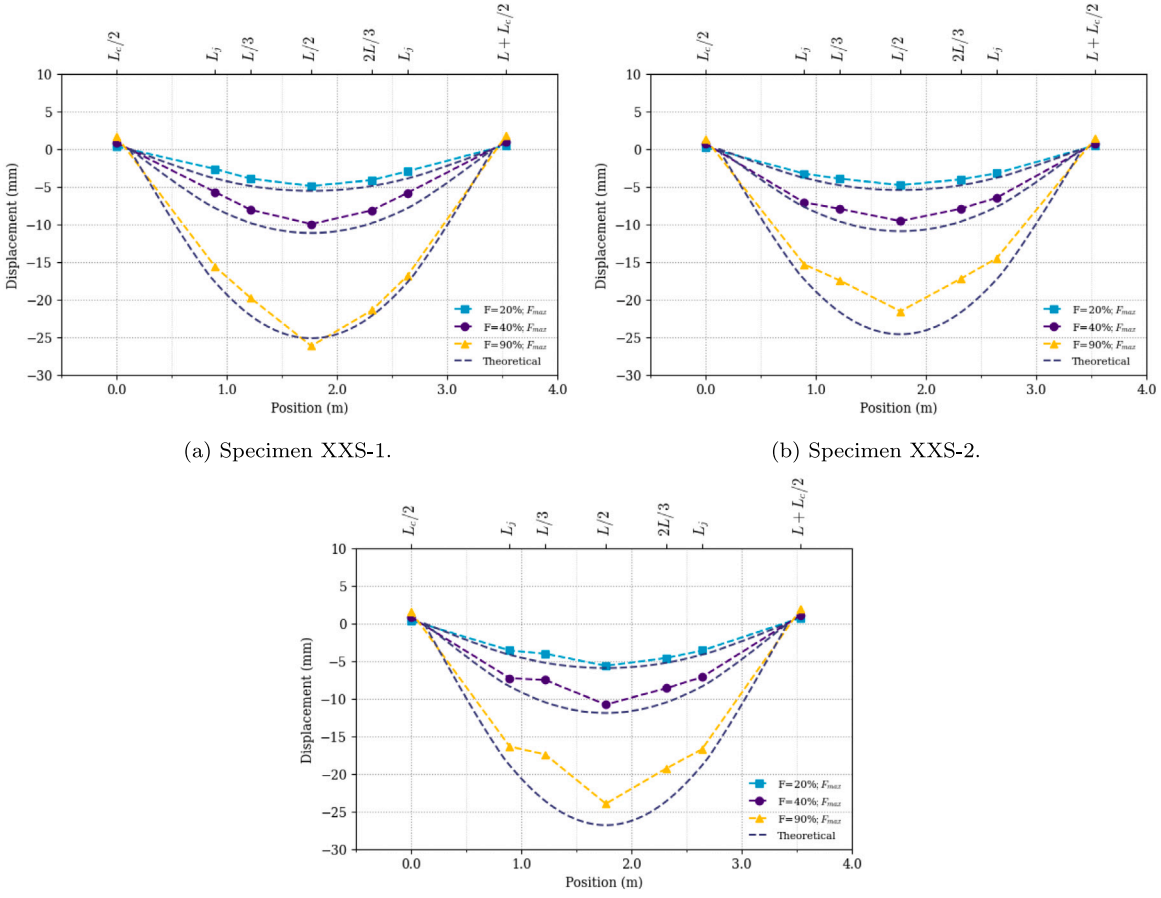


(a) Joint detachment and distortion at the column support.



(b) View of the alternative side after testing, including split failure at castellated joints.

Fig. 12. Alternative view of the specimen after testing including column joint distortions.



(a) Specimen XXS-1.

(b) Specimen XXS-2.

(c) Specimen XXS-3.

Fig. 13. Evolution of beam deflections in XXS specimens. Comparison between analytical and experimental responses.

introduced by the castellated tabs, the two panels meeting at the joint rotate approximately as rigid bodies, so that the relative horizontal displacement between matching points on either side of the joint varies linearly with their vertical position. The procedure comprised the following steps:

1. Three pairs of reference points were selected from the DIC speckle field. Each pair consisted of a point on the left-hand side of the joint and its counterpart on the right-hand side, located at the same vertical coordinate (Fig. 17(d)). The pairs were distributed at three different heights across the depth of the joint, within regions of intact speckle pattern, and away from the immediate vicinity of the castellated tabs where the displacement field is dominated by local geometric effects rather than by the overall joint rotation.
2. For each pair $i = 1, 2, 3$ and at every recorded frame, the horizontal displacements $u_{L,i}$ and $u_{R,i}$ were extracted from the DIC output and their difference $\Delta u_i = u_{R,i} - u_{L,i}$ was computed.
3. At each frame, the three values of Δu_i were plotted against the vertical coordinate y_i of the corresponding pair (Fig. 17(c)) and a straight line was fitted by linear least-squares regression. The joint rotation, θ at that frame was then taken as the slope of the fitted line, with the small-angle approximation $\theta \approx \tan\theta$ being adequate given that the measured rotations were of the order of 10^{-3} rad.
4. Steps 2 and 3 were repeated across all recorded frames to produce the rotation history of the joint, which was then paired with the corresponding moment derived from the actuator force to yield the moment–rotation relationships shown in Figs. 17(a) and 17(b).

It should be noted that, owing to a malfunction of one of the cameras during testing, the DIC records of the XXS specimens were corrupted and an experimental estimate of k_r could not be obtained for this group. The corresponding rotational stiffness is instead recovered from the calibrated finite element model and discussed in Section 4.

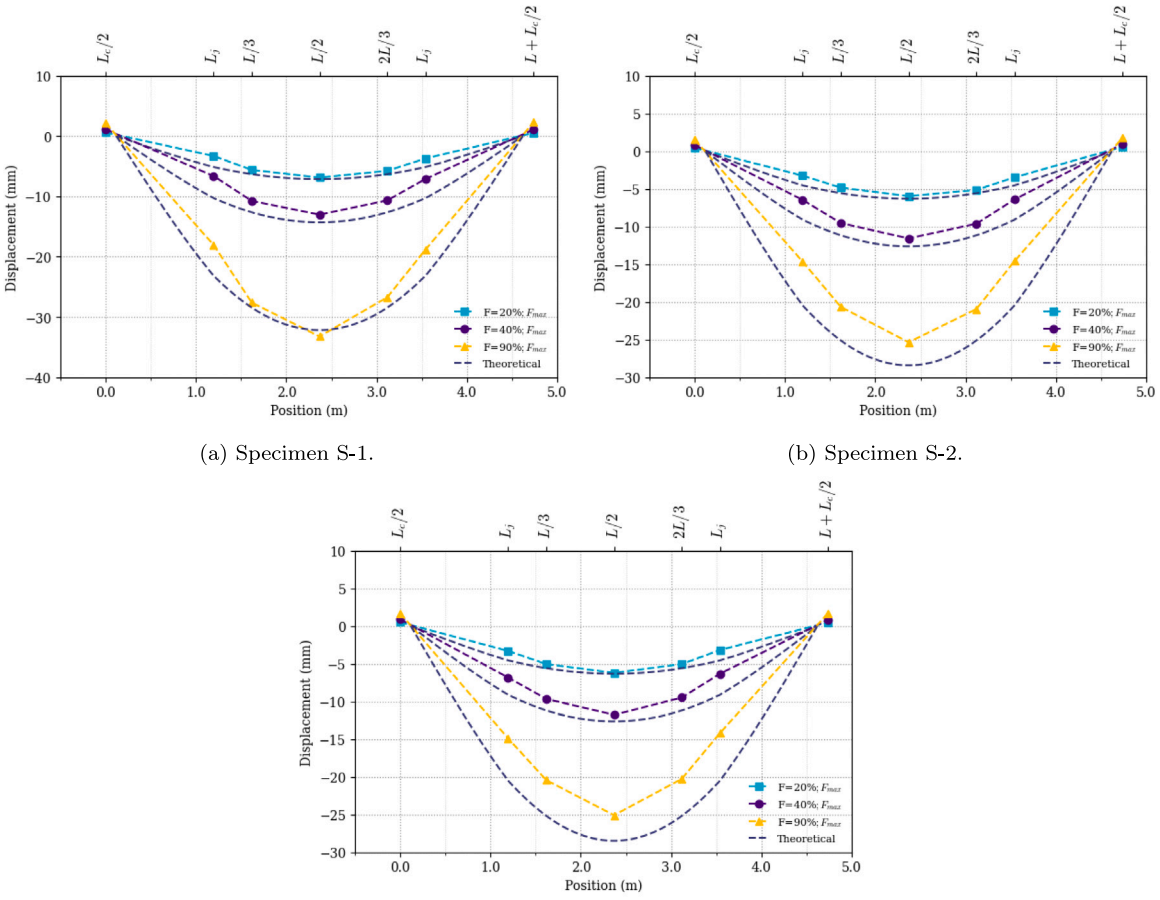
Finally, the value k_r to be used in Eq. (3) was derived via Eq. (4):

$$k_r = \frac{M_{40\%} - M_{10\%}}{rot_{40\%} - rot_{10\%}} \tag{4}$$

where $M_{40\%}$ and $M_{10\%}$ are the values of moment corresponding to 40% and 10% of the moment capacity, and $rot_{40\%}$ and $rot_{10\%}$ are the correlated rotation values.

The moment–rotation relationships obtained using this method are presented in Fig. 17(a) for the S-1 specimen and in Fig. 17(b) for the L-1 specimen. Unfortunately, the data for XXS specimens were corrupted due to a malfunctioning of the camera. The value of k_r was estimated to be equal to 3034 kNm/rad for the L-1 specimen and equal to 1800 kNm/rad for the S-1 specimen.

The previously presented Figures (13 to 15) have included the deflection estimations obtained from the analytical model described above and expressed by Eq. (3). These comparisons show that the proposed model represents fairly well the deflection for specimens XXS and S specimens. However, the deflection of specimens L is consistently over estimated. Some of the mismatch between measured and estimated deformed shapes can be attributed to construction tolerances and localised differential displacements that will alter the moment of inertia of the section in different ways along the beam length. It should be noted that the analytical model is but a simple idealisation of a more complex reality whose main assumptions are: (i) the rotation



(a) Specimen S-1.

(b) Specimen S-2.

(c) Specimen S-3.

Fig. 14. Evolution of beam deflections in S specimens. Comparison between analytical and experimental responses.

behaviour of the castellated joints is assumed to be elastic, and (ii) panels are assumed to be in full contact at the beginning of the analysis. In reality, there are small gaps between panels due to construction tolerances. The elastic relationship in the joint, therefore, is a highly idealised model for a mechanical contact-based model that is highly nonlinear. Nevertheless, given the complexity of the structure under consideration, a simple analytical model of the sort just introduced has a good practical merit in preliminary practical calculations. For more detailed analyses, advanced modelling approaches, like Finite Element formulations can be used. These models will be introduced in the next section.

4. Numerical modelling

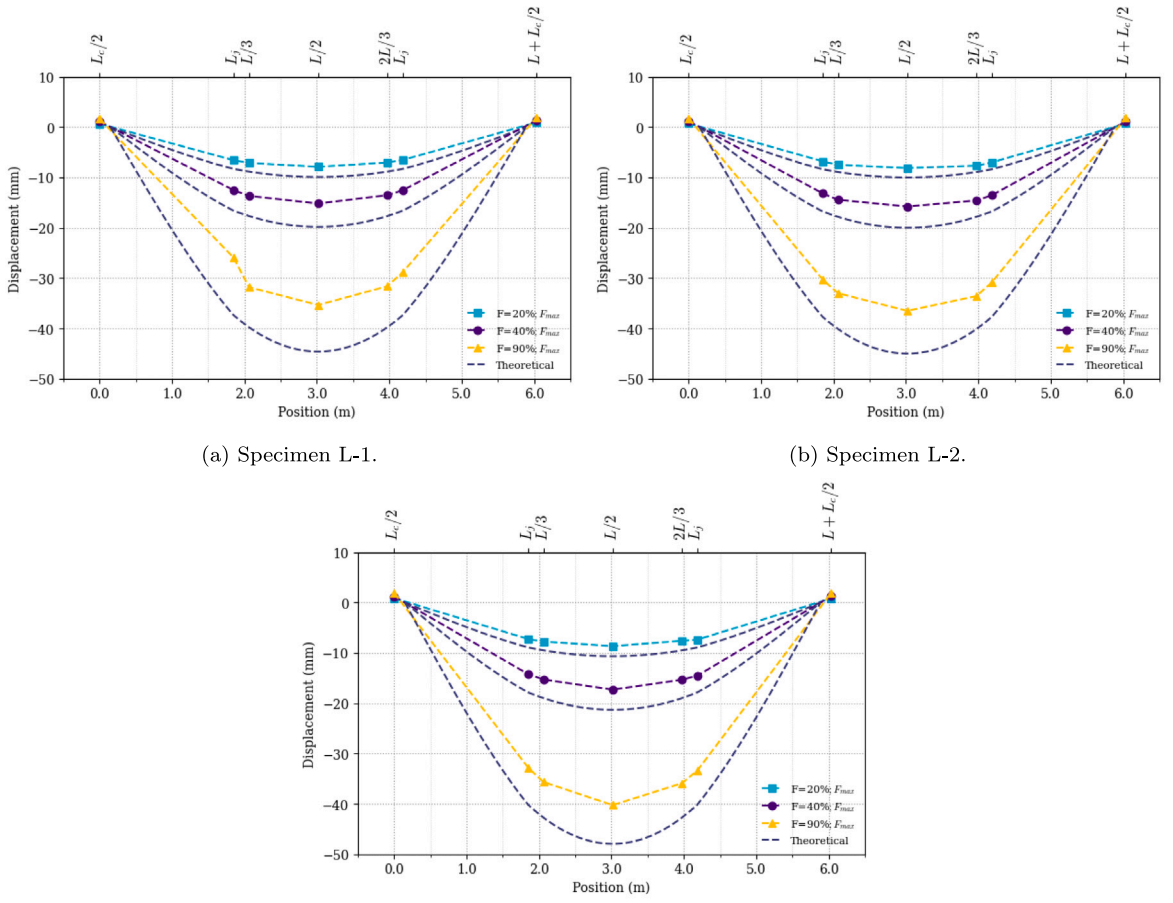
The experimental results presented in the preceding section were employed to validate detailed finite element models, enabling verification of the behavioural trends and mechanisms identified during testing. The general purpose finite element analysis package ABAQUS [15] was used for all numerical simulations reported herein. The following sections describe the modelling process and its results. This model is intended to capture the global response of the beams including their stiffness, joint stress concentration and fracture initiation. It does not intend to reproduce strand-scale material behaviour or fracture propagation, therefore, a homogeneous material model with equivalent elastic properties is assumed for the OSB. No model parameters were adjusted to match the experimental results; all material properties and contact parameters were assigned independently from material characterisation tests and literature values, and the model predictions were subsequently compared against the full experimental dataset.

4.1. Modelling assumptions

The geometric properties reported in Fig. 3 have been used to formulate the FE models. To this end, Rhino files containing the volumetric description of the beams were obtained from WIKI-House [10] and imported into ABAQUS (Fig. 18). The geometry was discretised using 8-node linear elements with reduced integration (C3D8R). A global element size of approximately 10 mm was adopted, with further refinement in regions of expected stress concentration such as joints and corners, as explained in Section 4.2. It should be noted that while the mesh in sensitive regions was defined based on the methods described later (Eq. (10)), a mesh sensitivity study was also conducted confirming that using a mesh size of less than 10 mm in the coarser regions leads to less than a 4% difference in the predicted peak forces.

Interaction between parts was considered by defining ‘hard’ and ‘friction’ surface interaction properties. A master–slave surface designation was used according to the stiffness and mesh densities, ensuring stable force transfer. And a ‘hard’ surface contact pressure over-closure relationship was defined in the normal direction to enforce no-overlapping between contact surfaces. And contact between adjacent OSB panels was modelled using a Coulomb friction formulation, following approaches commonly adopted in finite element modelling of timber and wood-based systems [16,17] with a friction coefficient of 0.25 as informed by preliminary sensitivity analyses.

A homogenous material with equivalent elastic properties was used to model the Oriented Strand Board (OSB) material. To this end, the modulus of elasticity (MOE) used was taken from the compressive material tests performed by [12]. Although Chen and He [18] reported differences in the MOE values in tension and compression for OSB,



(a) Specimen L-1.

(b) Specimen L-2.

(c) Specimen L-3.

Fig. 15. Evolution of beam deflections in L specimens. Comparison between analytical and experimental responses.

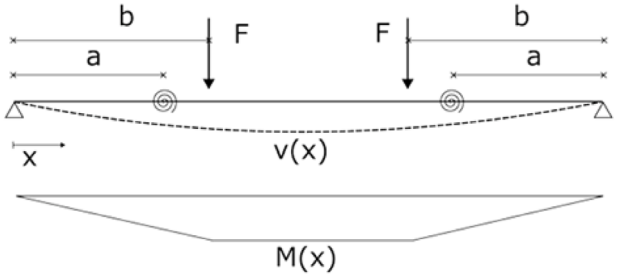


Fig. 16. Schematic representation of the structural model for the analytical formulation (top) and bending moment (bottom).

adopting a single value for structural modelling is a reasonable simplification. This assumption is consistent with our findings presented later, as well as with other studies showing that differences of this magnitude produce negligible variation in predicted structural capacities in other systems using OSB [19]. It is recognised, however, that OSB in tension will show an elastic-brittle response, whereas plasticity can develop in OSB under compression. To account for this, without over complicating the numerical model, an elastic plastic response was defined to allow some potential re-distribution of stresses that may be caused by the ductile compressive response, while tracking of the tensile strains was implemented to define potential fracture initiation via fracture mechanics concepts as discussed in the following section. Finally, an MOE of 2933 MPa corresponding to the average of the compression and tension MOEs, with a yield stress of 8.3 MPa corresponding to the tensile strength of the material, and a 10% hardening used merely for numerical stability were adopted. It should be noted that, since the analysis is terminated at the onset of cracking, the hardening modulus has little effect on the final response.

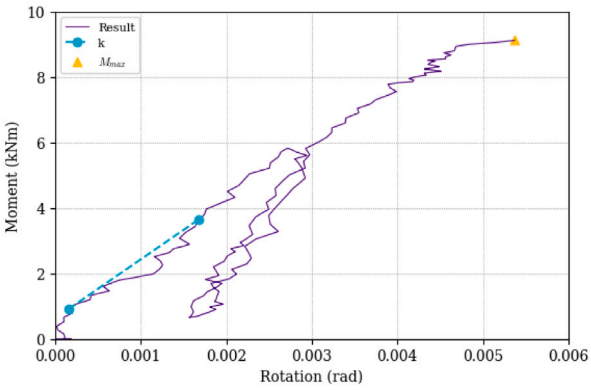
The structural model was constrained and loaded to replicate the four point experimental test. Therefore, loading was applied using a displacement controlled approach with distributed loads along the width of the beam applied at two thirds, as in the test. Similarly, support were simulated by providing hard constraints but allowing uplift at the ends of the column studs over the full section.

4.2. Modelling of fracture initiation

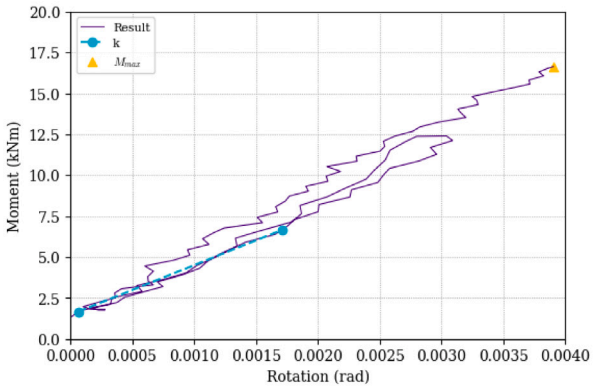
As noted above, our FE models do not explicitly incorporate damage or fracture formulations. To estimate the onset of failure, a fracture-based post-processing approach was adopted. Specifically, the mean stress method, based on linear elastic fracture mechanics (LEFM), was used to evaluate crack initiation at selected critical regions [20]. To this end, the stress field is integrated along a potential fracture path and the resulting mean stress is compared with a critical energy-based threshold to identify the likely onset of cracking. The corresponding load level is then taken as a proxy for the upper bound of the structural capacity in the absence of an explicit damage model.

Crack initiation is assumed to occur when a mixed-mode fracture criterion $f(G) \geq 1.0$. In the present work, the crack initiation index is defined in energy terms as:

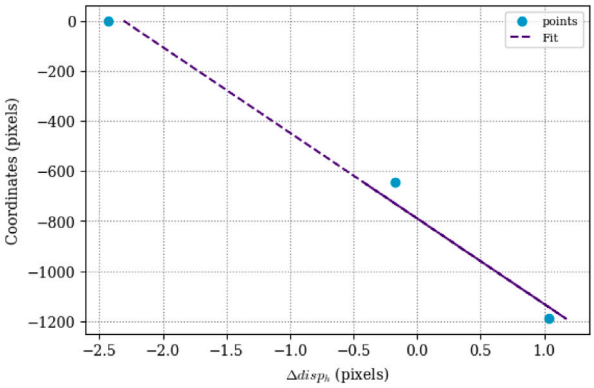
$$f(G) = \sqrt{\frac{G_I}{G_{I,c}} + \frac{G_{II}}{G_{II,c}}}. \tag{5}$$



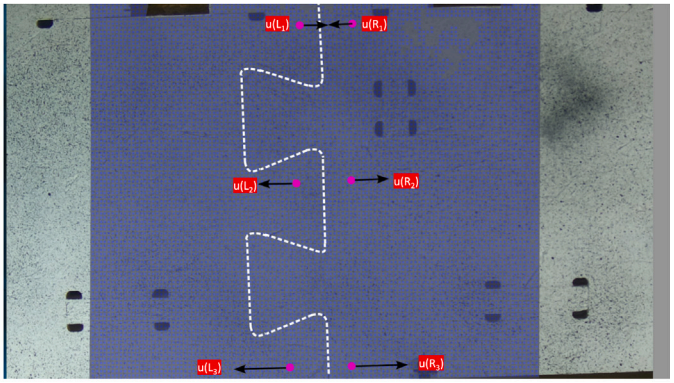
(a) Moment-rotation for the dovetail joint in S-1.



(b) Moment-rotation for the dovetail joint in L-1.



(c) Coordinates versus horizontal displacement.



(d) Position of coordinates.

Fig. 17. Moment–rotation of the castellated joint.

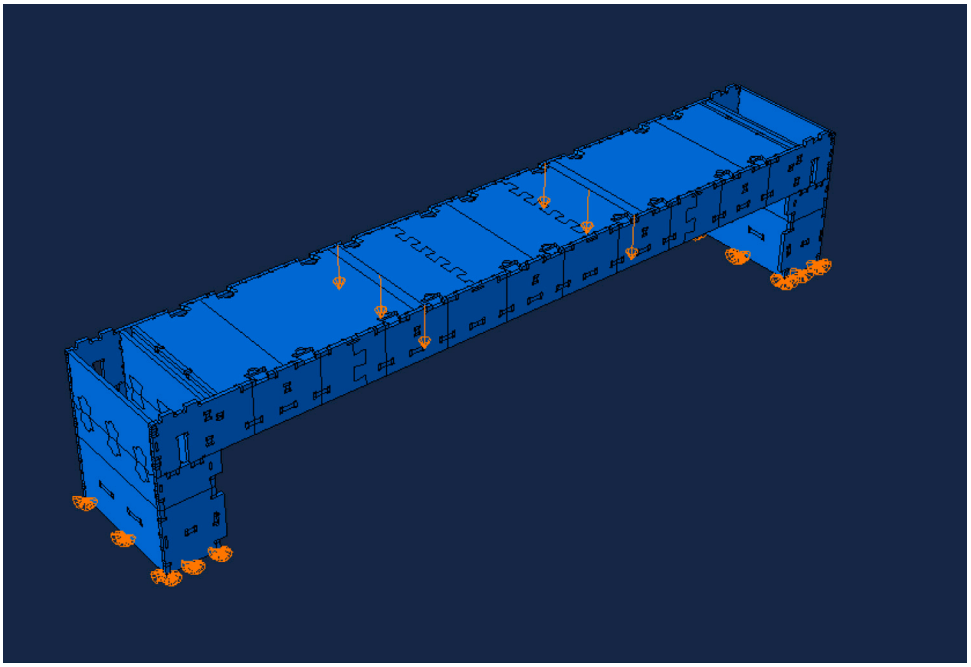


Fig. 18. General view of the FE model of Beam L. Support boundary conditions are shown as orange constraints at the bottom of the vertical studs while arrows indicate the loading direction on the numerical specimen.

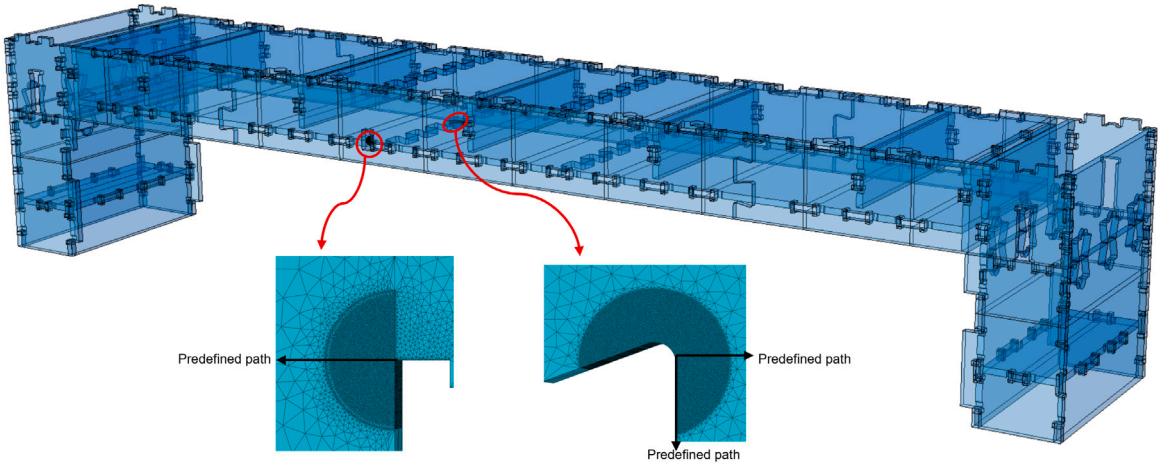


Fig. 19. Finer mesh discretisation around critical regions (castellated joints at bottom flange and stitched joints in lateral faces) used for fracture analysis.

where G_I and G_{II} are the mode I and mode II strain energy release rates. In the present OSB panel formulation, mode I corresponds to crack opening driven by tensile stresses normal to the assumed crack plane, while mode II corresponds to crack sliding driven by in-plane shear stresses along the assumed crack path. The adopted value of $G_{I,c} = 400$ N/m is consistent with reported Mode-I fracture energy measurements for OSB panels. Rathke et al. [21] reported an average specific fracture energy of approximately 400 J/m^2 (1 J/m^2 = 1 N/m). The value of $G_{II,c} = 1000$ N/m was adopted as a representative lower-bound estimate based on reported Mode-II fracture energy values for timber and wood-based materials [22], which are commonly of the order of 1.0–1.7 N/mm.

Since the OSB material is treated as an orthotropic engineered wood-based panel, the material axes x and y correspond to the major and minor panel directions of the board, respectively. The fracture assessment is therefore expressed using the OSB panel principal axes and the local coordinates of the assumed crack path, rather than using the grain-based terminology usually adopted in timber.

These energy release rates are linked to the classical stress intensity factors through the orthotropic generalisation of linear elastic fracture mechanics. For crack paths aligned with the OSB panel principal directions, the relations can be written as:

$$G_I = \frac{\sigma^2_{n,\text{mean}} \pi x_0}{2E^*_I}, \qquad G_{II} = \frac{\tau^2_{ns,\text{mean}} \pi x_0}{2E^*_{II}}. \tag{6}$$

where the normal stress acting perpendicular to the assumed crack plane, σ_n, and the in-plane shear stress acting along the assumed crack path, τ_{ns}, are extracted along this path from the finite element results and averaged over a characteristic length x_0, yielding the mean stresses $\sigma_{n,\text{mean}}$ and $\tau_{ns,\text{mean}}$. The terms E^*_I and E^*_{II} are generalised elastic moduli accounting for the orthotropic elastic response of OSB. Following the orthotropic LEFM formulation, these moduli can be expressed as:

$$E^*_I = \sqrt{\frac{2E_{xx}E_{yy}}{\sqrt{E_{xx}/E_{yy}} - \nu_{xy} + E_{xx}/(2G_{xy})}}, \tag{7}$$

$$E^*_{II} = \sqrt{\frac{2E^2_{xx}}{\sqrt{E_{xx}/E_{yy}} - \nu_{xy} + E_{xx}/(2G_{xy})}}, \tag{8}$$

where E_{xx} and E_{yy} are the elastic moduli along the OSB major and minor panel directions, respectively, G_{xy} is the in-plane shear modulus, and ν_{xy} is the in-plane Poisson's ratio.

A key component of the mean stress method is the introduction of a characteristic length x_0, representing the extent of the high-stress region over which stresses are averaged. Combining the above expressions provides an explicit relation for the mean stress length x_0 as:

$$x_0 = \frac{2}{\pi}\frac{K^2_I}{f^2_{t,n}}\left[1 + \frac{(K_{II}/K_I)^2}{(f_v/f_{t,n})^2}\right]. \tag{9}$$

where $f_{t,n}$ denotes the tensile strength of the OSB panel in the direction normal to the assumed crack plane, f_v denotes the in-plane shear strength, and K_I and K_{II} are stress intensity factors [23]. In this application, x_0 was obtained through an iterative process, where the assumed value was progressively adjusted to match the right-hand side of the equation. The resulting value was approximately 10 mm which falls within the range of typical values for mean stress length reported in [24]. In practice, the stress field obtained from the finite element analysis is extracted along the assumed crack path, mean stresses are evaluated over a prescribed length x_0, and the load level at which $f(G)$ first reaches unity is interpreted as the onset of cracking.

For the fracture analysis of the OSB beams tested, local mesh refinement was applied to resolve the stress concentrations at critical locations. To reduce computational cost, refinement was restricted to two dominant stress-concentration regions: (i) the interface between the two bottom plates on the underside, and (ii) the loaded region around the frontal notch. Fig. 19 shows the finer mesh discretisation around these critical regions, including the castellated joints at the bottom flange and the stitched joints in the lateral faces used for the fracture analysis.

A sufficiently fine mesh is required in the vicinity of stress concentrations. Accordingly, a circular mesh refinement scheme is adopted around stress concentration zones. The refinement is characterised by a radius $r_{\text{FE,refined}}$ and a minimum element size at the corner, defined as:

$$\rho_{\text{FE},i} = \frac{x_0}{300}, \tag{10}$$

resulting in a minimum element size of 0.04 mm in the refined region. This mesh size was used to provide sufficient resolution for extracting the mean stresses over the characteristic length x_0 [25].

Taking the analysis of the XXS beam as an example, in the vicinity of the stitched joint, Fig. 20 shows the average stresses evaluated along the assumed crack path and used to compute the fracture index $f(G)$ at successive loading stages. It was found that $f(G) = 1.0$ was reached at a load between 12.4 kN and 13.0 kN, suggesting that crack initiation is likely to occur within this load interval.

5. Numerical results

Fig. 21 compares the experimentally obtained force–displacement relationships with the results of our numerical simulations. An excellent

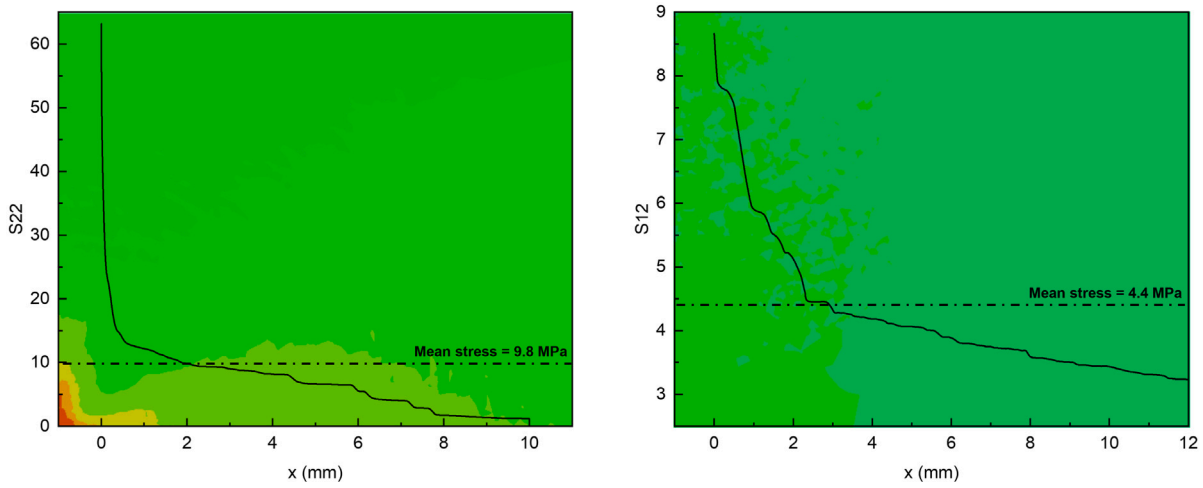
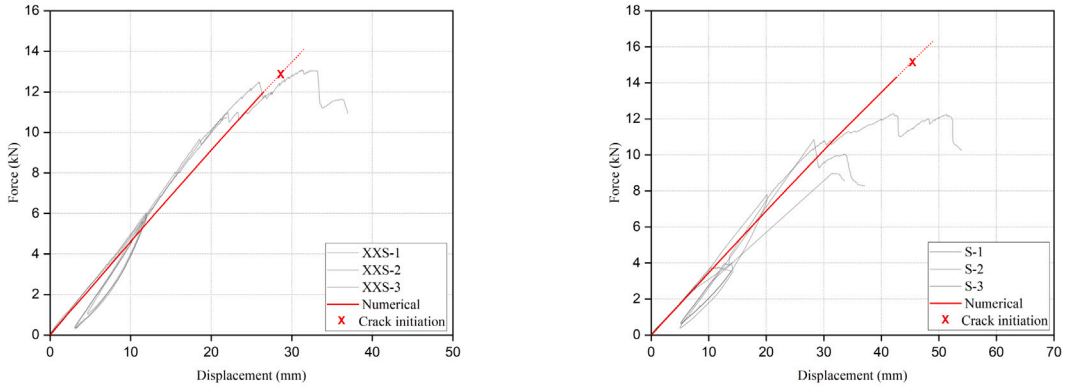
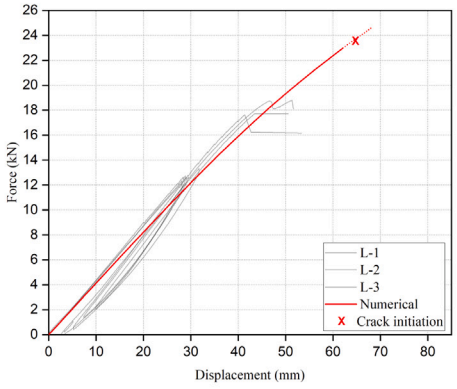


Fig. 20. Example of the calculated average mean stresses at the vicinity of one stitched joint in beam XXS.



(a) Specimens XXS.

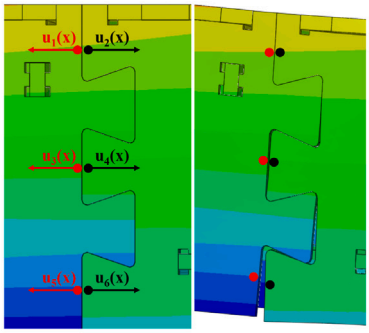
(b) Specimens S.



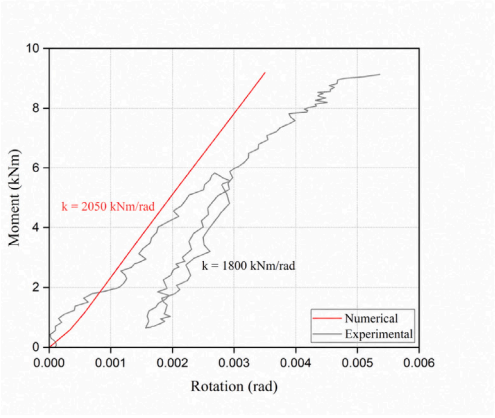
(c) Specimens L.

Fig. 21. Comparison of numerical and experimental (grey lines) global force–displacement relationships for all specimens tested. The red line represents numerical predictions divided between response before fracture (continuous read line) with the dashed red line indicating fracture region with the cross marking the most likely fracture capacity as determined by the FE model.

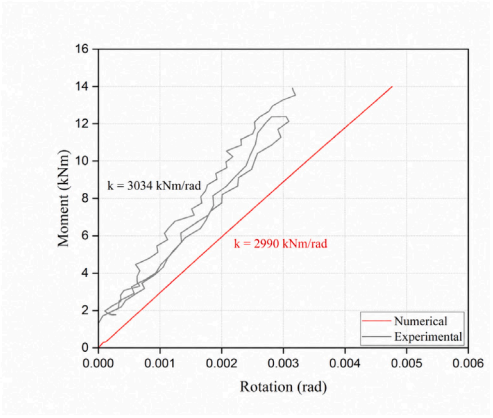
estimation of stiffnesses and its evolution is evident in this figure, confirming the modelling assumptions adopted. Fig. 21 also shows a clear trend in the mean-stress-based crack initiation prediction: from XXS to S and L, the predicted crack initiation point shifts to slightly higher forces and larger displacements. For the XXS beams, the predicted crack initiation point is relatively close to the experimental peak-load region, indicating that the adopted mean stress approach provides a reasonable estimate of the onset of fracture in the smaller specimens. However, especially for L beams, the predicted crack initiation force becomes noticeably higher than the experimental peak load.



(a) Position of reference nodes in the FE model for the rotation calculation.



(b) Moment-rotation comparison in beam S.



(c) Moment-rotation comparison in beam L.

Fig. 22. Comparison of numerical and experimental moment–rotation relationships at the dovetail joints.

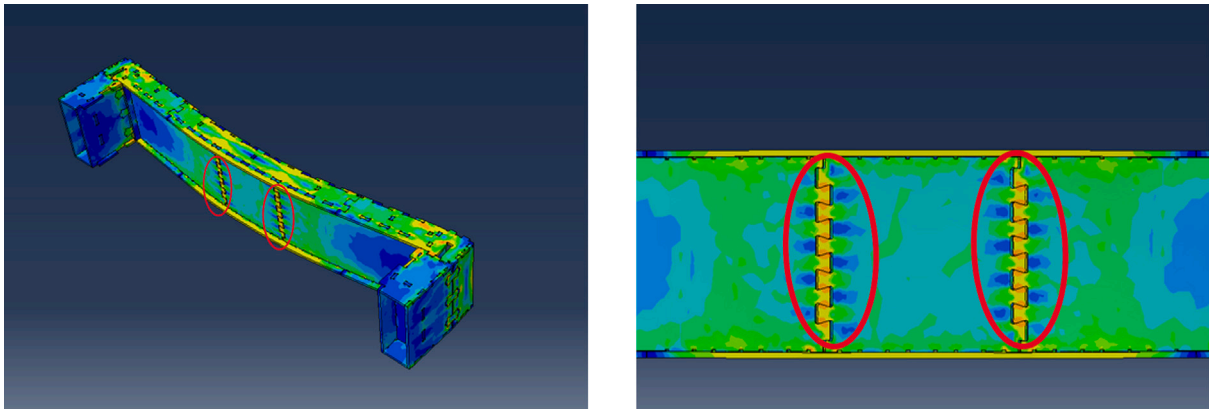


Fig. 23. FEA model predicting failure of beam XXS at castellated joint.

This trend is consistent with the fact that the present fracture assessment identifies local crack initiation, while the experimental peak load reflects the onset of global structural degradation. It is reasonable to expect that the global response of longer beams is more strongly influenced by the accumulation of unavoidable assembly tolerances, initial gaps, contact slip, uneven bearing, and local redistribution of forces between adjacent interlocking regions; since small local misalignments can accumulate over a larger span and reduce the effective contact area between panels. As a result, the same global bending demand may generate higher local tensile and prying stresses at the bottom castellated joints than those predicted in the idealised FE model, causing cracking and strength degradation to occur earlier in the experiments. Nonetheless, overall, the results support the use of the mean stress method as a fracture-informed indicator for crack initiation, while also highlighting the complexities of measuring and modelling contact-based imperfections in interlocking structures.

5.1. Moment–rotation at dovetail joints

It is also of interest to compare the numerical moment–rotation curves with their experimentally obtained counterparts presented in the previous section. To this end, the same method used during the experimental data processing was adopted. As shown in Fig. 22(a), three pairs of points were selected on either side of the castellated joint, and their horizontal displacements were extracted. The differences

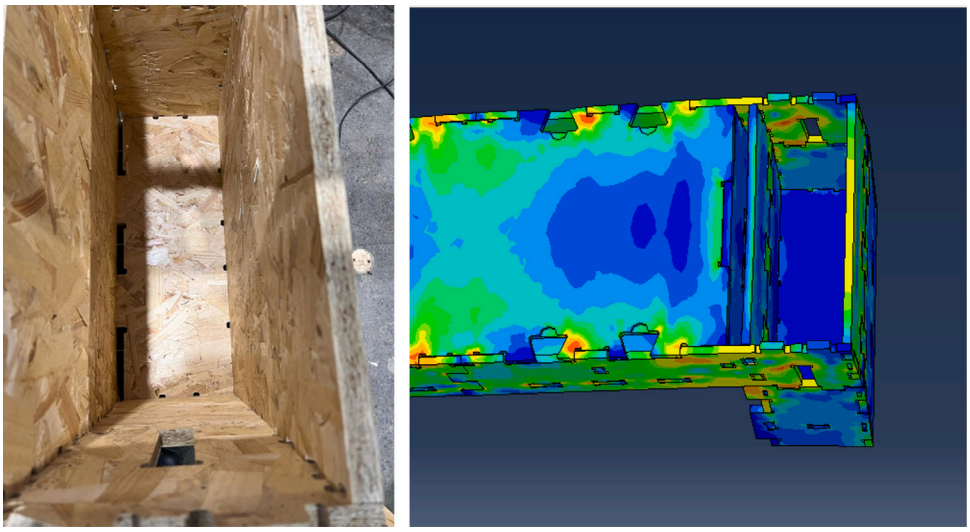


Fig. 24. Column distortions are observed when the applied load approaches the beam strength eventually leading to bowing and buckling initiation. The experimental response is well replicated by the FE model.

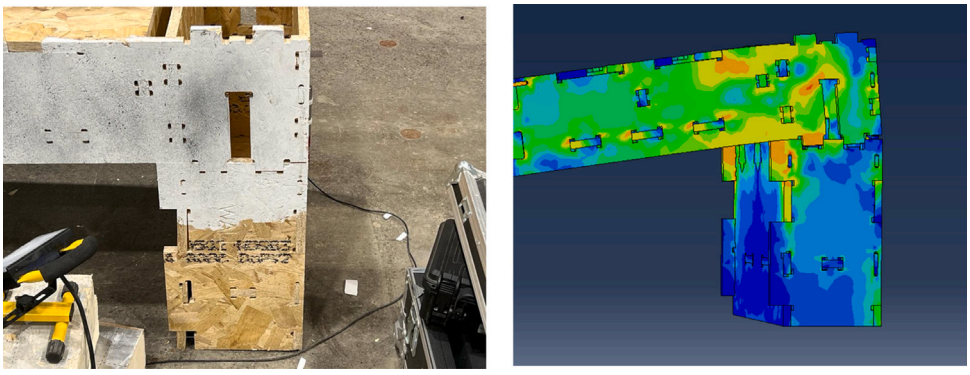


Fig. 25. Vertical separation and tearing at the beam–column interface as observed and simulated.

between these displacements were then used in a regression analysis to determine the corresponding rotation angle.

The comparison between the numerical and experimental results is presented in Figs. 22(b) and 22(c). For the L beam, the main difference in moment is observed at the initial stage leading to a discrepancy between the two curves. However, generally good agreement between the numerical and experimental results can still be observed in terms of overall rotational stiffness. The fitting in this region is satisfactory, with errors in rotational stiffness of +13.8% for the S beam and −1.4% for the L beam. Finally, for the XXS beam, whose rotational stiffness was not possible to obtain experimentally, a stiffness of 1279 kNm/rad was derived from the numerical model. A comparison among the three numerical cases indicates that the rotational stiffness increases with increasing span.

5.2. Stress concentration in castellated joints

Observations during testing and the subsequent numerical simulations indicate that castellated joints are critical stress concentration points that govern the overall beam response through crack initiation. For instance, Beam XXS-1 exhibited initial cracking at the right-hand side of the bottom castellated joint immediately before failure while Beam XXS-2 failed initially at the left-hand side of the castellated joint. Subsequent Digital Image Correlation (DIC) analysis confirmed that stress concentrations associated with cracking were attained on both sides of the castellated joint in Beam XXS-2 nearly simultaneously, but damage progressed quickly on the left. By contrast, fracture in Beam XXS-3 initiated at the centre of the joint. Our FE analysis correlates strongly with these observations. As shown in Fig. 23 high tensile stresses appear around the castellated joints closely matching the experimental observations. As, expected, given the lack of in-situ imperfection measurements and their implementation in the numerical model. This is evidenced by the fact that tensile failure is reached uniformly in these joints. Overall, the experimental and numerical findings collectively indicate that the castellated joints, while serving a mechanical purpose in assembly or interlocking, can dominate the early stages of failure. Similar responses and observations were made for Beams S and L. It should be noted that, given the nature of the model and its assumptions, no out of plane tensile failure on the webs of the beam would be predicted, as observed experimentally when pushing the beams beyond the initial tensile fracture of the castellated joints. This is due to the failure definition adopted which renders any post-failure results unobservable. However, the FE was able to reproduce other behavioural mechanisms, as discussed below.

5.2.1. Column tab distortions

Fig. 24 shows the experimentally and numerical contact state and distortions between the tab slots at the bottom of the right column in Specimen S during loading. Also observed was a gradual inward bowing of the column sidewalls. These features are indicative of compressive deformations followed by mild shear-induced wall instability. Once the lower interface failed, the load path through the column panel became eccentric, causing local buckling at very large demands. This response is well replicated by the FE models. Besides, looking further

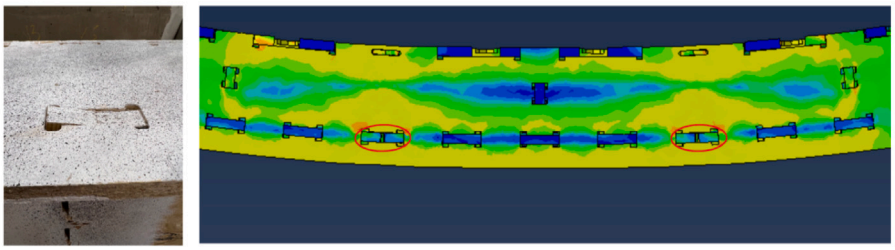


Fig. 26. Experimental and numerical observation of localised slot tearing, vertical splitting, and progressive joint opening.

at the columns (Fig. 25), the vertical separation and tearing at the beam–column interface indicate that the column could not maintain full bearing contact as deformation increased. This was observed both during testing and in the numerical analysis.

5.2.2. Tearing of slotted joints

In some cases, the beam rotation and horizontal shear forces that concentrated along the castellated joint, produced tension and prying stresses that exceeded the capacity of the thin OSB wall. This resulted in localised slot tearing, vertical splitting, and progressive joint opening, consistent with separation-driven failure in thin-walled composite connections. This can be seen in Fig. 26 where the castellated joint of both the left and right sides of beam L and its corresponding FE model.

All the previously discussed results and comparisons give confidence in the modelling strategy. The proposed FE models can be used in future studies to complement the experimental findings described herein.

6. Conclusions

Nine monotonic four-point bending tests on full-scale CNC-cut OSB Skylark beam specimens have been reported in this paper. This is the first experimental and numerical investigation of digitally-manufactured OSB tubular beams assembled according to the open-source Skylark system, which relies solely on interlocking joints for its load-carrying capacity, making it an attractive sustainable housing solution. The experimental campaign was supplemented by simplified analytical calculations of deflection and by three-dimensional finite element models. The principal findings and conclusions are summarised below:

- The castellated joints in the bottom flange consistently govern the bending strength of OSB Skylark beams. All specimens failed in a brittle manner initiated by tensile fracture at these joints, identifying the bottom-flange castellated connection as the critical design region for this system.
- The mean moment capacities recorded were 6.9 kNm for the XXS beams (3.3 m span), 8.0 kNm for the S beams (4.5 m span), and 17.1 kNm for the L beams (5.74 m span). Good repeatability was observed across all three beam types, providing confidence in the reliability of the test data.
- Column uplift was consistently observed during testing, indicating that significant bending moment was transferred from the beam to the short columns acting as end supports. This behaviour should be accounted for in the design and detailing of support conditions in practical applications.
- The three-dimensional FE model with linear fracture initiation criteria proposed in this study successfully reproduces the main behavioural mechanisms observed experimentally, including the location and character of failure initiation. Although relying on maximum tensile stress limits for failure identification and not intended to model crack propagation or damage accumulation, our model captures the load–displacement response and failure point with good accuracy across all beam sizes.
- The analytical deflection model, based on semi-rigid rotational joint representations consistent with approaches used in timber structures with flexible connections, provides reasonable estimates of beam stiffness and can serve as a practical tool for preliminary design.
- Based on both experimental and numerical observations, it can be concluded that the castellated joints in the bottom flange of the beam play a key role in the determination of the bending strength of these beams suggesting that joint detailing governs the bending strength of these beams.

Several aspects of the present study warrant further consideration. The experimental dataset covers three section geometries and a single OSB grade, and the FE models assume idealised contact conditions at the interlocking joints. The influence of contact imperfections introduced during panel cutting or assembly has not been quantified, and the investigation is restricted to monotonic loading. Therefore, future work should prioritise the characterisation of individual castellated joints in isolation, the sensitivity of structural response to manufacturing tolerances and contact imperfections, extension to alternative OSB grades and panel thicknesses, and assessment of behaviour under cyclic loading. System-level validation of floor assemblies and wall-to-floor connections remains a necessary step towards full structural certification of the Skylark platform for multi-storey housing applications.

CRediT authorship contribution statement

Christian Málaga-Chuquitaype: Writing – original draft, Writing – review & editing, Supervision, Resources, Methodology, Investigation, Formal analysis, Conceptualization. **Opeyemi Ogunkuade:** Writing – review & editing, Investigation, Formal analysis. **Zilan Zhang:** Writing – review & editing, Investigation, Formal analysis. **Gabriele Granello:** Writing – review & editing, Methodology, Formal analysis.

Declaration of competing interest

The authors declare that they have no known competing financial interests or personal relationships that could have appeared to influence the work reported in this paper.

Acknowledgments

The authors wish to express their warmest gratitude to Mr. Leslie Clark of the Imperial College Structures Laboratory and Ms. Li (Elizabeth) Yang for their invaluable assistance during the execution of the experiments reported in this paper.

Data availability

Data will be made available on request.

References

[1] U. Habitat, World cities report: The value of sustainable urbanization. United Nations Human Settlements Programme, 2020, URL https://unhabitat.org/sites/default/files/2022/06/wcr_2022.pdf.

[2] R. Haigh, L. Li, Decade review of modular construction systems in the building and construction industry: research trends toward the development and utilisation of timber materials within the context of a circular economy, Wood Mater. Sci. Eng. (2026) 1–20.

[3] H.-T. Thai, T. Ngo, B. Uy, A review on modular construction for high-rise buildings, in: Structures, vol. 28, Elsevier, 2020, pp. 1265–1290.

[4] C. Robeller, Y. Weinand, Interlocking folded plate–integral mechanical attachment for structural wood panels, Int. J. Space Struct. 30 (2) (2015) 111–122.

[5] C. Robeller, A. Stitic, P. Mayencourt, Y. Weinand, Interlocking folded plate: integrated mechanical attachment for structural wood panels, in: Advances in Architectural Geometry 2014, Springer, 2014, pp. 281–294.

[6] A. Stitic, C. Robeller, Y. Weinand, Experimental investigation of the influence of integral mechanical attachments on structural behaviour of timber folded surface structures, Thin-Walled Struct. 122 (2018) 314–328.

[7] A. Rezaei Rad, Y. Weinand, H. Burton, Experimental push-out investigation on the in-plane force-deformation behavior of integrally-attached timber through-tenon joints, Constr. Build. Mater. 215 (2019) 925–940.

[8] A.C. Nguyen, Y. Weinand, Development of a spring model for the structural analysis of a double-layered timber plate structure with through-tenon joints, in: Proc. World Conf. Timber Engineering (WCTE 2018), 2018.

[9] A. Rezaei Rad, H.V. Burton, Y. Weinand, Macroscopic model for spatial timber plate structures with integral mechanical attachments, J. Struct. Eng. 146 (10) (2020) 04020200.

[10] Open Systems Lab, WikiHouse: An open-source construction system. URL https://www.wikihouse.cc.

[11] G. Granello, T. Reynolds, C. Prest, Structural performance of composite WikiHouse beams from CNC-cut timber panels, Eng. Struct. 252 (2022) 113639.

[12] G. Granello, Material Testing of Metsa Plywood and Sterling OSB, Tech. Rep., 2021, URL https://www.wikihouse.cc/research/material-testing-of-metsa-plywood-and-sterling-osb.

[13] CEN, Comité Européen de Normalisation, EN 408, CEN, timber structures—structural timber and glued laminated timber—determination of some physical and mechanical properties, 2012.

[14] CEN, BS EN 1380:2009 Timber structures. Test methods. Load bearing nails, screws, dowels and bolts, 2009.

[15] Dassault Systemes Simulia Corporation, Abaqus, 2014, Providence, Rhode Island, USA.

[16] V. Karagiannis, C. Málaga-Chuquitaype, A. Elghazouli, Behaviour of hybrid timber beam-to-tubular steel column moment connections, Eng. Struct. 131 (2017) 243–263.

[17] L. Sirumbal-Zapata, C. Málaga-Chuquitaype, A. Elghazouli, Experimental assessment and damage modelling of hybrid timber beam-to-steel column connections under cyclic loads, Eng. Struct. 200 (2019) 109682.

[18] G. Chen, B. He, Stress-strain constitutive relation of OSB under axial loading: An experimental investigation, BioResources 12 (3) (2017) 6142–6156.

[19] C. Kyprianou, P. Kyvelou, L. Gardner, D.A. Nethercot, Finite element modelling of sheathed cold-formed steel beam–columns, Thin-Walled Struct. 183 (2023) 110365.

[20] P.J. Gustafsson, Mean stress approach and initial crack approach, in: Fracture mechanics models for analysis of timber beams with a hole or a notch–a report of RILEM TC-133, Report TVSM-7134, Lund University, Sweden, 2002.

[21] J. Rathke, G. Sinn, M. Harm, A. Teischinger, M. Weigl, U. Müller, Fracture energy vs. internal bond strength–mechanical characterization of wood-based panels, Wood Mater. Sci. Eng. 7 (4) (2012) 176–185.

[22] S.A. Rahman, M. Subhani, M. Ashraf, Mode-II progressive fracture of sawn timber and timber-adhesive bond: Experimental evaluation of end notched flexure (ENF) testing using DIC, Eur. J. Wood Wood Prod. 81 (6) (2023) 1437–1453.

[23] G.R. Irwin, Analysis of stresses and strains near the end of a crack traversing a plate, J. Appl. Mech. 24 (3) (1957) 361–364.

[24] M. Detter, G. Hochreiner, J. Füssl, An engineering approach to evaluate stress concentrations at openings in CLT shear walls, Eng. Struct. 343 (2025) 121249.

[25] M. Detter, G. Hochreiner, M. Lukacevic, J. Füssl, FEM-based engineering approach to assess the bearing strength of glt members with holes and notches, in: Proceedings from the 14th World Conference on Timber Engineering (2025), 2025, pp. 2138–2146.